

# Visualization of mouse spinal cord intramedullary arteries using phase- and attenuation-contrast tomographic imaging

Yong Cao,<sup>a</sup> Xianzhen Yin,<sup>b</sup> Jiwen Zhang,<sup>b</sup> Tianding Wu,<sup>a</sup> Dongzhe Li,<sup>a</sup> Hongbin Lu<sup>c\*</sup> and Jianzhong Hu<sup>a\*</sup>

Received 14 January 2016

Accepted 17 April 2016

Edited by J. F. van der Veen

**Keywords:** intramedullary arteries; phase-contrast imaging; attenuation-contrast imaging; high resolution.

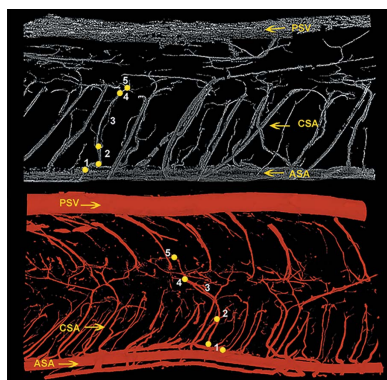
<sup>a</sup>Department of Spine Surgery, Xiangya Hospital, Central South University, Changsha 410008, People's Republic of China, <sup>b</sup>Center for Drug Delivery System, Shanghai Institute of Materia Medica, Chinese Academy of Sciences, Shanghai 20203, People's Republic of China, and <sup>c</sup>Department of Sports Medicine, Research Centre of Sports Medicine, Xiangya Hospital, Central South University, Changsha 410008, People's Republic of China.

\*Correspondence e-mail: hongbinlu@hotmail.com, jianzhonghu@hotmail.com

Many spinal cord circulatory disorders present the substantial involvement of small vessel lesions. The central sulcus arteries supply nutrition to a large part of the spinal cord, and, if not detected early, lesions in the spinal cord will cause irreversible damage to the function of this organ. Thus, early detection of these small vessel lesions could potentially facilitate the effective diagnosis and treatment of these diseases. However, the detection of such small vessels is beyond the capability of current imaging techniques. In this study, an imaging method is proposed and the potential of phase-contrast imaging (PCI)- and attenuation-contrast imaging (ACI)-based synchrotron radiation for high-resolution tomography of intramedullary arteries in mouse spinal cord is validated. The three-dimensional vessel morphology, particularly that of the central sulcus arteries (CSA), detected with these two imaging models was quantitatively analyzed and compared. It was determined that both PCI- and ACI-based synchrotron radiation can be used to visualize the physiological arrangement of the entire intramedullary artery network in the mouse spinal cord in both two dimensions and three dimensions at a high-resolution scale. Additionally, the two-dimensional and three-dimensional vessel morphometric parameter measurements obtained with PCI are similar to the ACI data. Furthermore, PCI allows efficient and direct discrimination of the same branch level of the CSA without contrast agent injection and is expected to provide reliable biological information regarding the intramedullary artery. Compared with ACI, PCI might be a novel imaging method that offers a powerful imaging platform for evaluating pathological changes in small vessels and may also allow better clarification of their role in neurovascular disorders.

## 1. Introduction

The spinal cord is the primary information pathway connecting the peripheral nerves to the brain, and acts as a center for some simple reflex pathways (Goto & Otsuka, 1997). The normal physiological activity of the spinal cord relies on the organized distribution and integrity of intramedullary arteries, which present a unique and intricate three-dimensional (3D) morphology. The central sulcus arteries that supply nutrition to a large part of the spinal cord are the most important arteries maintaining the normal function of the spinal cord (Martirosyan *et al.*, 2011). Some vascular disorders related to the spinal cord, including angiogenesis in tumors and congenital vascular malformation and embolization in spinal cord blood vessels, are typically associated with chaotic distribution and dysfunction of the microvasculature (Niimi *et*



© 2016 International Union of Crystallography

*al.*, 2015; Gandhi *et al.*, 2015; Garg *et al.*, 2015). Thus, under these conditions, the blood flow and the oxygen and nutrient delivery to the neurons will be affected and cause irreversible damage to spinal cord function. In addition, substantial evidence from pathological and clinical studies suggests that these circulatory disorders are triggered by small vessel lesions with diameters of less than 10  $\mu\text{m}$  (Rubin & Rabinstein, 2013). Therefore, the detection of such small vessel lesions will facilitate the early diagnosis and potentially more effective management of these disorders, resulting in better outcomes.

A number of imaging methodologies for the diagnosis of spinal cord vasculature diseases have been developed and reported. The intramedullary arteries, which are typically less than 10  $\mu\text{m}$  in diameter, are below the detection limit of conventional radiography techniques, such as digital subtraction angiography (DSA), clinical computed tomography angiography (CTA) and magnetic resonance angiography (MRA), due to the limited imaging resolution of these techniques (Uotani *et al.*, 2008; Mori *et al.*, 1996; Zhang *et al.*, 2013). These modalities are all suitable for the detection of large vascular malformations with diameters of 200  $\mu\text{m}$  (Mori *et al.*, 1996; Zhang *et al.*, 2013). Tissue sectioning with light microscopy provided high resolution for vascular imaging, but failed to capture the 3D nature of the vascular architecture (Figley *et al.*, 2014). Two-photon microscopy or ultrastructural methods such as scanning electron microscopy (SEM) have been available for 3D rendering of the spinal cord vasculature. But these methods are incapable of providing a quantitative 3D characterization at the microscopic level. Two-photon imaging microscopy has depth-of-field imaging limits, and SEM is incompatible with studies of the intact spinal cord or a living organism (Koyanagi *et al.*, 1993a,b; Tang *et al.*, 2015; Kerschensteiner *et al.*, 2005). Micro-computed tomography is a powerful 3D imaging tool that allows detection of the 3D morphology of vessels at high resolutions. Although quantitative parameters of the vessel morphology can be ascertained using this technique, the method cannot effectively image vessels with diameters of less than 20  $\mu\text{m}$  (Hu *et al.*, 2012).

Recently, the development of synchrotron radiation (SR), which is characterized by high monochromatic photon flux and sufficient coherence, has become a new detection technique in the field of biomedical imaging (Suortti & Thomson, 2003; Lewis, 1997). Two main imaging models are used for third-generation SR in medical applications. In addition to conventional attenuation-contrast imaging (ACI) based on variations in tissue densities, the phase-contrast imaging (PCI) model is a novel imaging method developed in recent years (Eggl *et al.*, 2015; Hoshino *et al.*, 2014). PCI is based on Fresnel diffraction, which can record the phase shifts imposed by the X-ray wave penetrating the specimen. Its sensitivity is approximately 1000-fold higher than that of ACI, and the method elicits higher contrast information regarding the biomedical sample architecture, even when the attenuation-contrast differences are imperceptible (Zhou & Brahme, 2008; Momose *et al.*, 1996; Lundström *et al.*, 2014). Data on 3D tumor vessel visualization and brain vessel detection in preclinical tests generated by ACI and PCI combined with

tomography have been published (Xuan *et al.*, 2015; Zhao *et al.*, 2012; Lang *et al.*, 2012; Myojin *et al.*, 2007). However, the combination of PCI and ACI based on SR for the high-resolution tomography of the intramedullary arteries of the spinal cord has not been conducted previously.

In this study, we investigated the imaging efficiency of the combination of ACI and PCI based on SR for the detection of the intramedullary arteries in the mouse spinal cord. The imaging qualities of these two imaging models for the high-resolution tomographic microscopy of the arteries, particularly the characteristics of the central sulcus arteries, were also evaluated and compared.

## 2. Materials and methods

### 2.1. Animals and study design

All of the experiments performed in this study were approved and conducted in compliance with the guidelines established by the Animal Care and Use Committee of the Central South University. A total of 24 C57BL/6J mice were randomly divided into three groups ( $n = 8$  in each group). Group A underwent immunofluorescence staining, group B underwent ACI, and group C underwent PCI.

### 2.2. Sample preparation

The animals in group A were euthanized with an overdose of 10% chloral hydrate and then subjected to a thoracotomy followed by a heparinized saline (500 ml) perfusion through the circulatory system *via* the ascending aorta to allow effective draining of the blood flow. Subsequently, fresh spinal cord samples at the level of the tenth thoracic spinal vertebra with a length of 4 cm were harvested and fixed with 4% paraformaldehyde in PBS (pH 7.4) at room temperature (RT) for 3 h.

After heparinized saline perfusion, the animals in groups B and C were subjected to vessel network fixation with 10% buffered formalin through the ascending aorta. The animals in group B were subjected to contrast agent perfusion with Microfil (MV-122, Flow Tech, CA, USA) for ACI scanning according to previously described methods (Hu *et al.*, 2012). Briefly, a proportional mixture of contrast agents (Microfil MV-122, Flow Tech, CA, USA) was infused into the ascending aorta *via* a perfusion pump with a filling rate of 0.5 ml min<sup>-1</sup> at 140 mmHg for 5 min. The rats in group C did not undergo contrast agent perfusion for PCI scanning. Thereafter, all of the animals in groups B and C were maintained at 4°C overnight. The following day, the T10 thoracic cord segment with a length of 5 mm was harvested and fixed in a 10% buffered formalin solution. Twenty-four hours later, all of the specimens were dehydrated with a gradient of ethyl alcohol for 12 h and then prepared for scanning.

### 2.3. Immunofluorescence staining

The samples in group A were cryoprotected with 6% sucrose/PBS overnight, rinsed with acetone, embedded in optimal cutting temperature compound (OCT) (Sakura

**Table 1**  
Comparative analysis imaging parameters for ACI and PCI.

Imaging parameters	ACI	PCI
Sample-to-detector distance (cm)	2	30
Exposure time (s)	2.5	2.5
Scanning energy (keV)	15	15
Projection images	720	720
Dark-field images	5	5
Flat-field images	12	12
CCD ( $\mu\text{m pixel}^{-1}$ )	$1.625 \times 1.625 \times 1.625$	$1.625 \times 1.625 \times 1.625$

Finetek USA) and cut into 5  $\mu\text{m}$ -thick sections. The sections were then blocked with 10% goat serum in PBS for 1 h to block non-specific binding, and then incubated with a mouse monoclonal RECA-1 antibody (1:200; Abcam plc, Cambridge, UK) diluted in 3% goat serum in PBS overnight at 4°C. After washing three times with PBS, the sections were incubated with the secondary antibody, Cy3 goat anti-mouse IgG (H+L) (1:1000; Jackson, USA), diluted in 3% goat serum for 30 min at RT. The sections were washed with PBS, counter-stained with DAPI and were then mounted using an anti-fade mounting medium and examined with an Olympus BX60 microscope. The results were photographed using *Picture Frame* software (Optronics) and compared with the vascular images obtained using SR imaging.

### 2.4. SR imaging

SR scanning was performed using the BL13W1 beamline experimental station of the Shanghai Synchrotron Radiation Facility (SSRF). The sample was fixed on the rotary stage, which was exposed to the SR light path. Subsequently, the SR light transmitted through the object was detected by a charge coupled device (CCD) camera with  $1.625 \times 1.625 \times 1.625 \mu\text{m}$  pixels (Photonic Science, UK) (Fig. 1). As shown in Fig. 2, as X-rays traverse a sample, rapid variations in the refractive index deviate the X-rays by angles that can be detected by adjusting the detector at a certain distance from the object. More details of the experimental parameters used in ACI and PCI tomography imaging are listed in Table 1. For comparison, we performed ACI- and PCI-based computed tomography (CT) scanning, including projection, flat-field and dark-field image acquisitions. For both ACI- and PCI-based CT scanning, the entrance dose added to the tissue sample was

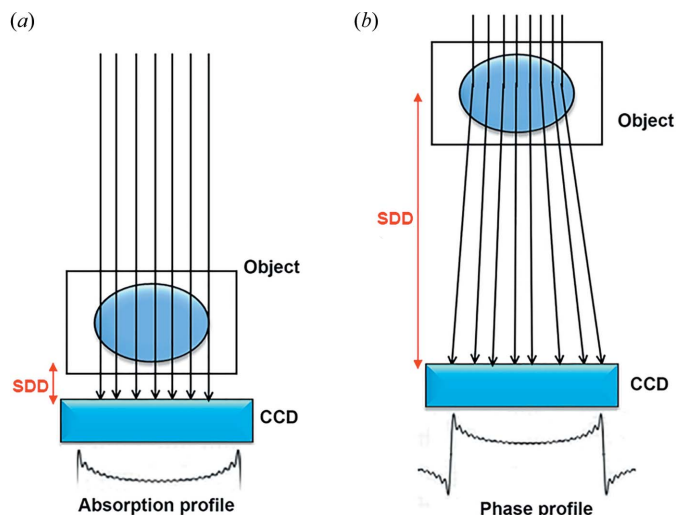


**Figure 2**  
Schematic depiction of the phase contrast theory of SR. In a typical SR scan, the object is placed very close to the detector as in the ACI setup (a), whereas in a phase contrast setup the object is placed at a distance from the detector (b). SDD = sample to detector distance.

approximately 1.065 Gy per projection. Subsequently, all initial projection images were transformed to digital slice sections using the *GPU-CT-Reconstruction* software (applied by the BL13W1 Experimental Station) based on the filtered back projection (FBP) algorithm. A series of slices was reconstructed using the *VG Studio Max 3D* reconstruction software (version 2.1, Volume Graphics GmbH, Germany) to render 3D images.

### 2.5. Image analysis

In the ACI slices, the vessels filled with contrast agents were identified as the areas with high gray values. Inversely, the vascular lumen was distinguished from the surrounding neural parenchyma by its low gray values in the PCI slices. Because the scan specimen location was the same for the ACI and PCI scans and the axial direction of the transverse slice reconstruction procedures was also identical, the two scanned datasets could be simply matched by registering the top and bottom image slices. To confirm the imaging efficiency of ACI and PCI, a corresponding immunofluorescence slice from a location near those of the ACI and PCI slices was selected for comparison. To evaluate the correlation among these methods

in two dimensions (2D), 24 randomly selected blood vessels in slices from similar locations in each dataset were analyzed. The vessel diameter (VD) and angle were calculated using the *Image-Pro Plus (IPP)* software program (version 6.0; Media Cybernetics, Bethesda, MD, USA). In 3D, to evaluate the local differences in the vessel parameters, spinal specimens of the same length filled with a vascular structure were selected from each tomography dataset. An algorithm for

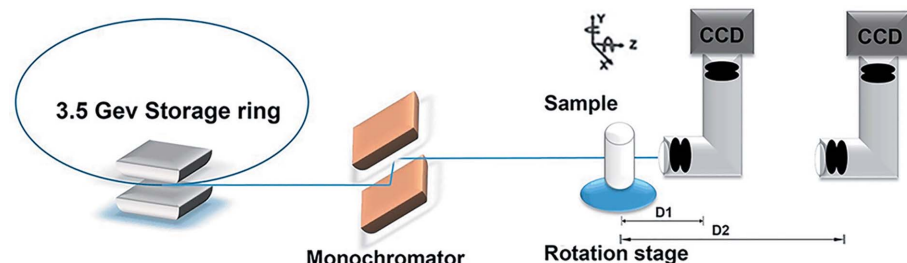


**Figure 1**  
Schematic depiction of the BL13W1 beamline experimental station in SSRF. The sample-to-detector distance (SDD) can be varied from 0.05 m to a maximum of 8 m. The image can be recorded at several distances by adjusting the SDD.

vessel morphology quantification developed in MATLAB 7.10.9 R2010a as described by Lang *et al.* (2012) was used for evaluating the differences between these two methods.

### 2.6. Statistical analysis

The data are presented as the means  $\pm$  standard error. The statistical analyses were performed using the SPSS software package (version 17.0; University of Cambridge, Cambridge, UK). The differences in the image quality generated by the different imaging techniques were analyzed using a two-tailed *t*-test after ascertaining a normal distribution with a Kolmogorov–Smirnov test or through an analysis of variance (ANOVA) with a *post hoc* Tukey–Kramer analysis. A *p* value of less than 0.05 was interpreted as statistically significant.

## 3. Results

### 3.1. Projection images of ACI and PCI

Fig. 3 shows the ACI and PCI projection images of the spinal cord intramedullary artery network. Due to the high

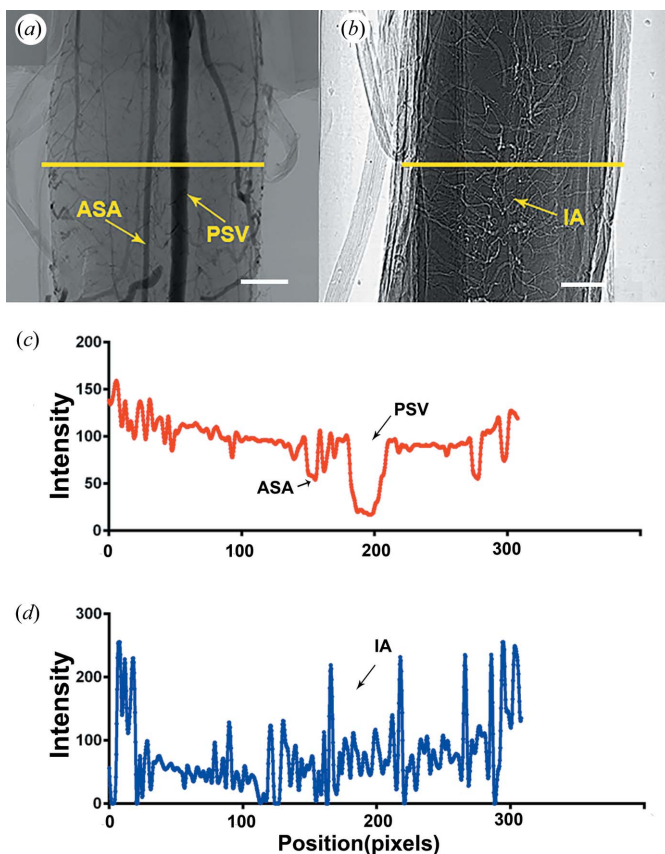


**Figure 3** Projection images detected by ACI ( $n = 8$ ) and PCI ( $n = 8$ ). (a) Projected ACI image. (b) Projected PCI image. (c, d) Comparison of the density distributions of the cross-sectional profiles marked in (a) and (b). (c) The attenuated signal decreased significantly, indicating the location of the anterior spinal artery (ASA) and posterior spinal vein (PSV) marked in (a). (d) The fluctuations in the line profiles in (a) and (b) are frequent in areas of the spinal cord enriched with an intramedullary artery (IA) network. (a, b) Scale bar: 100  $\mu\text{m}$ .

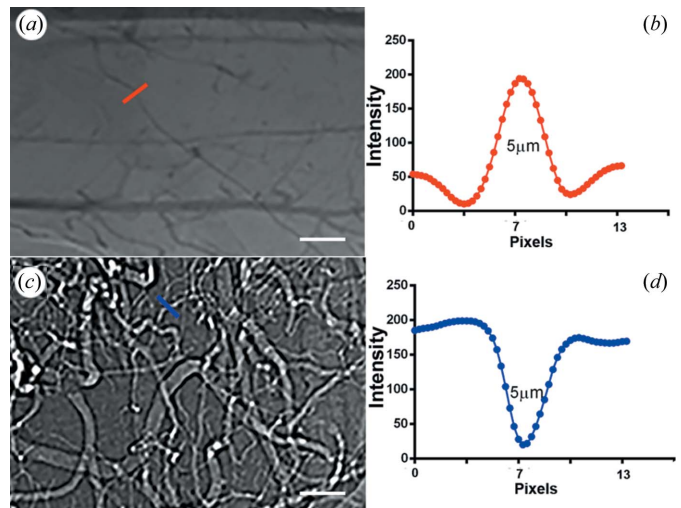


**Figure 4** Local details of the intramedullary artery network detected by PCI ( $n = 8$ ) and ACI ( $n = 8$ ). (a) PCI images. (c) ACI images. (b) Profile along the yellow line in (a). (d) Profile along the blue line in (c). (a, b) Scale bar: 50  $\mu\text{m}$ .

absorbance efficiency of the contrast agent, the artery filled with contrast agent can be detected on the ACI images (Fig. 3a), and the dense small vessels in the cord parenchyma, as well as the large arteries and veins in the cord membrane, can be distinguished from the surrounding tissue background. The images in Fig. 3(b) demonstrate that the intramedullary artery was clearly visualized without contrast agent perfusion on the PCI images. The intensity distribution of the line profiles (yellow line profile) marked in Figs. 3(a) and 3(b) are illustrated in Figs. 3(c) and 3(d), indicating the location of the vessel. The local details of the intramedullary artery are shown in Figs. 4(a) and 4(c). The vessel boundaries were detected both with and without contrast perfusion, and appeared to overlap and form a dense vessel network in the neural parenchyma, and the smallest diameter detected in both the ACI and PCI images was approximately 5  $\mu\text{m}$  [Figs. 4(b) and 4(d)].

### 3.2. Comparative analysis of 2D slice images using a histological method

The transverse views of the immunofluorescence staining of the spinal cord indicated that the areas showing positive RECA-1 red staining reflected the vessel locations [Figs. 5(a) and 5(b)]. In the PCI tomography slices, areas with low gray values and high enhancement edge refraction, indicating a lack of contrast agent, were detected, and these correspond to the vascular lumen [Figs. 5(c) and 5(d)]. In contrast, the areas with high gray values, indicating X-ray opaque contrast injection into the vessel, were visible on the ACI slices [Figs. 5(e) and 5(f)]. The distributions of the vessel in the gray matter of the spinal cord on the 2D ACI and PCI slices largely matched those obtained from the immunofluorescence slices. To investigate any potential differences among ACI, PCI and

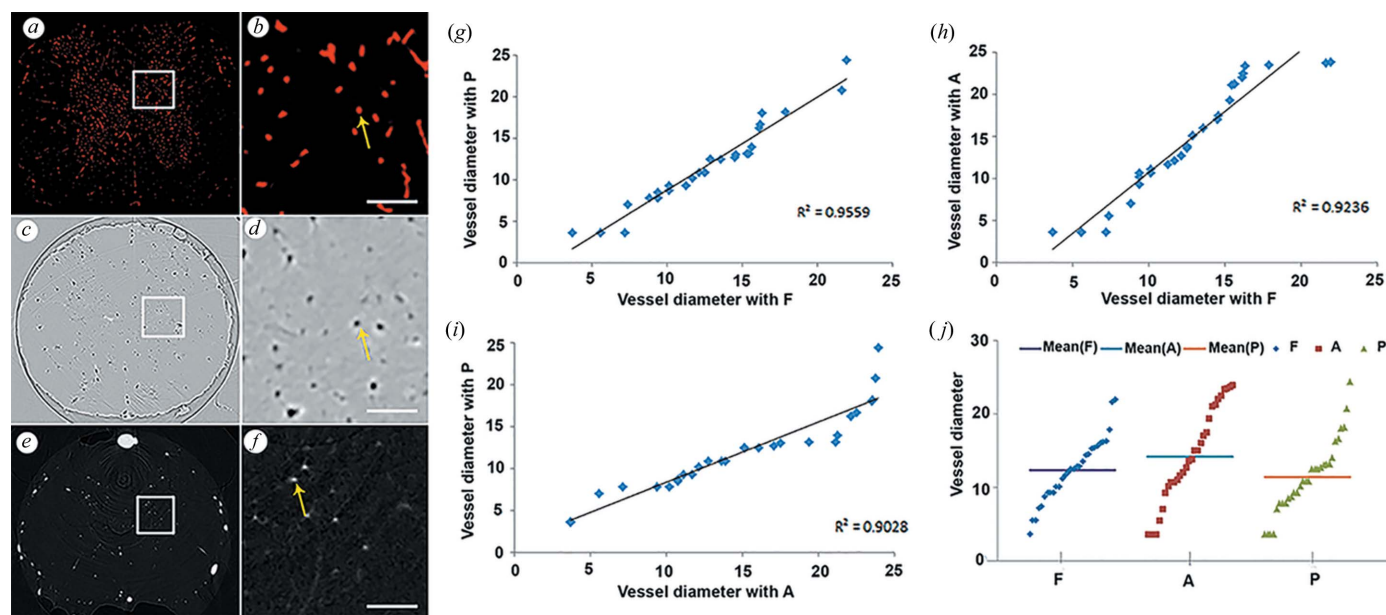


**Figure 5** Comparative analysis of the ACI and PCI slice images using the histological method. (a) Immunofluorescence staining of spinal cord microvessels ( $n = 8$ ). (c) PCI image of the spinal cord microvessels ( $n = 8$ ). (e) ACI image of the spinal cord microvessels ( $n = 8$ ). Panels (b), (d) and (f) show magnified images of the rectangles in (a), (c) and (e). (g) Correlation of vessel measurement between P and F ( $R^2 = 0.9559$ ). (h) Correlation of vessel measurements between A and F ( $R^2 = 0.9236$ ). (i) Correlation of vessel measurement between P and A,  $R^2 = 0.9208$ . (j) Mean diameter measurements obtained with F, A and P ( $P > 0.05$ ). Abbreviations: F = immunofluorescence imaging; A = ACI; P = PCI. Scale bar = 50  $\mu\text{m}$ .

immunofluorescence imaging in vessel visualization, the vessel diameter was automatically calculated using the plugin algorithms in *IPP*. The vessel diameter measured with PCI was highly correlated with that obtained through immunofluorescence imaging [ $R^2 = 0.9559$ ,  $P < 0.001$ ; Fig. 5(g)]. The correlation between the vessel diameter distributions obtained with ACI and immunofluorescence imaging was equally high [ $R^2 = 0.9236$ ,  $P < 0.001$ ; Fig. 5(h)], and the correlation between PCI and ACI presented similarly high values [ $R^2 = 0.9028$ ,  $P < 0.001$ , Fig. 5(i)]. Additionally, the average vessel diameter measurements obtained with ACI and PCI were similar to the measurements obtained with immunofluorescence imaging [ $P > 0.05$ ; Fig. 5(j)], which is the gold standard for vessel imaging. This result confirms the accuracy of the ACI and PCI reconstruction images and the corresponding equivalence of the ACI and PCI reconstruction slice data.

### 3.3. 3D images of the intramedullary artery in the unsectioned spinal cord

The 3D high-resolution images of the intramedullary artery generated by ACI and PCI are shown in Fig. 6. As shown, the images preserve the structural integrity of the spinal cord specimen and provide a precise configuration of the complex spatial structure associated with the intramedullary arteries. Due to the rim enhancement effect in PCI, the boundary and surface of the entire spinal cord are visible in the PCI images (red arrow) and could be rendered in 3D (Fig. 6a) but could not be detected in the ACI images (Fig. 6c). The fine details of the intramedullary artery were visualized throughout the spinal cord at high resolution in the ACI and PCI images. The

**Table 2**

Comparative analysis of the 3D morphology of the intramedullary artery between ACI and PCI ( $n = 8$  per group).

	ACI	PCI
Vessel numbers	$3673.38 \pm 647.45$	$3696.53.7 \pm 624.68$
Vessel volume ( $\text{mm}^3$ )	$0.36 \pm 0.05$	$0.37 \pm 0.87$
Vessel volume fraction (%)	$34.13 \pm 4.01$	$34.63 \pm 4.44$

vascular connectivities, shapes, densities and main branches could be clearly appreciated at multiple levels. In addition, the intramedullary arteries were mainly located in the gray matter and formed a butterfly shape, as demonstrated through both imaging techniques. The vessel density in the white matter was relatively lower [Figs. 6(a) and 6(c)].

To assess the imaging difference between ACI and PCI, the vessel diameters obtained using both imaging models were evaluated. The corresponding spinal cord segments in each dataset were selected, and we found no significant differences in the vessel diameter frequency distribution between ACI and PCI [ $P > 0.05$ ; Fig. 6(e)]. In addition, the vessel numbers (VN), vessel volume (VV) and vessel volume fraction (VVF) of the spinal cord intramedullary arteries, which were calculated from the PCI images, were similar to the morphology parameter measurements obtained from the corresponding ACI dataset (Table 2). For more detailed comparisons between these two imaging models, the characteristic artery of the spinal cord, the central sulcus artery (CSA), was systematically analyzed. From the sagittal plane of the spinal cord, we were able to visualize the CSA arising from the anterior spinal

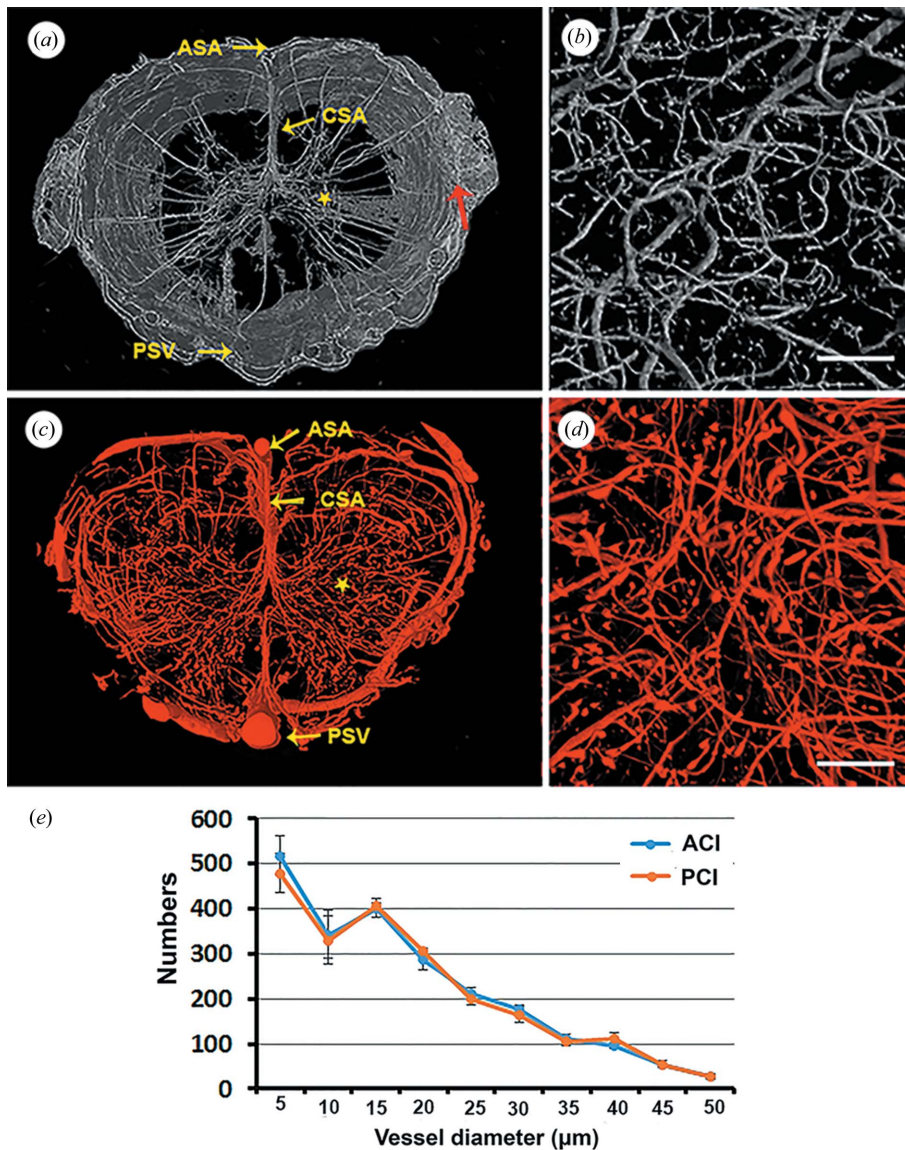


**Figure 6** 3D images of the intramedullary artery of the spinal cord obtained using PCI ( $n = 8$ ) and ACI ( $n = 8$ ). The images in (b) and (d) are magnified views of the gray matter area (yellow star) shown in (a) and (c), respectively. The final 3D vessel diameter distribution of the intramedullary artery extracted from the PCI dataset largely matched the results measured obtained with ACI ( $P > 0.05$ ). (b), (d) Scale bar = 50  $\mu\text{m}$ .

artery (ASA) at a certain angle and growing into the parenchyma, thus serving as the main nutritional supply to the spinal cord [Figs. 7(a) and 7(c)]. In the images obtained by ACI, the fifth branch of the CSA in the rat spinal cord was detected, whereas PCI was unable to distinguish the CSA at the same level [Figs. 7(b) and 7(d)]. Other vessel parameters, including the diameter and angle of the CSA, measured from the ACI and PCI images, are listed in Table 3. The ACI and the PCI dataset showed no significant differences in these parameters.

#### 4. Discussion

The laboratory mouse is used extensively in mammalian models for exploring genetic variation in preclinical human

disease research (Yuan *et al.*, 2011). The laboratory-based micro-CT system, which is a powerful 3D imaging tool, has successfully reconstructed the 3D morphology of the spinal cord microvasculature system. Nevertheless, vessels with diameters of less than 20  $\mu\text{m}$  cannot be detected due to physioptical limitations, such as geometric blur and low flux shortage within the X-ray light source (Hu *et al.*, 2012). However, without contrast agent perfusion, these vessels cannot be visualized using the laboratory-based micro-CT system. Although numerous studies have analyzed the cerebral artery in a mouse model through SR imaging, very few studies used this imaging method for detection of the mouse spinal cord microvasculature (Kidoguchi *et al.*, 2006; Zhang *et al.*, 2015; Stolz *et al.*, 2011). Moreover, the brilliant and highly monochromatic SR sources yield high-resolution PCI in biological specimens and have been explored as a novel method for vessel detection in various organ systems (Zhou & Brahme, 2008; Tang *et al.*, 2012).

In this study, we describe the imaging conditions for PCI and ACI based on SR. The intramedullary arteries of the spinal cord in a mouse model were successfully visualized using PCI and ACI. Combining these techniques with CT, we obtained an excellent 3D representation of the vessel structure of the intramedullary arteries within an unsectioned spinal cord, allowing the observer to examine the vessel morphology from multiple levels and perspectives (Zhang *et al.*, 2015). Hence,

this novel procedure could be used to trace the vessel along its entire course, allowing identification of the beginning and the end of the vessel. Furthermore, direct 3D quantitative morphometric data of vessel morphology could be extracted after a 3D image is obtained through both PCI and ACI. However, this work was challenging when using conventional methods, which provide only fragments that show 2D depictions of the vessel and are not appropriate for vessel quantification (Figley *et al.*, 2014). Although some geometric models of the vessel have been established for extrapolation of 2D analysis to 3D quantitative values, this method can yield unpredictable errors if the models are not verified. Additionally, more detailed analysis and further comparative work regarding spinal cord vessel visualization using the PCI and ACI methods are needed.

**Table 3**  
Comparative analysis of CSA imaging parameters between ACI and PCI.

	ACI	PCI
Minimum vessel size ( $\mu\text{m}$ )	5	5
Mean diameter of CSA ( $\mu\text{m}$ )	$8.36 \pm 1.09$	$8.325 \pm 0.87$
Number of CSA per $50 \mu\text{m}$	$6.63 \pm 1.06$	$6.75 \pm 0.92$
Mean angle of CSA ( $^\circ$ )	$72.25 \pm 7.96$	$72.5 \pm 5.42$
Branch level of CSA	5	5

In this manuscript, the imaging efficiencies and differences between PCI and ACI in the detection of the intramedullary artery microstructure of the spinal cord were systematically evaluated and compared. Our results confirm the high-resolution imaging ability of PCI and ACI for vessel structure visualization. Both of these methods could elicit more detailed information regarding vessel morphology on the microscale, particularly in mouse models. It is well known that many vascular diseases present the early development of small vascular lesions (Rubin & Rabinstein, 2013). Thus, the development of a high-resolution imaging method to capture the early anatomical structural changes of the vasculature during these diseases is desirable. However, understanding the concept of the vascular bed with micro-level specificity is a major challenge with the current conventional imaging methods (Uotani *et al.*, 2008; Zhang *et al.*, 2013). In our

experiments, the diameter of the smallest vessel identified was approximately  $5 \mu\text{m}$ , and this feature of the method could play a crucial role in the diagnosis of small vessel lesions and potentially aid the early diagnosis of spine disorders. Additionally, the morphology of the intramedullary artery in the PCI images matched that obtained from the ACI images and histology. As an imaging method, PCI allows much better discrimination of soft tissue than ACI (Eggl *et al.*, 2015; Hoshino *et al.*, 2014; Zhou & Brahme, 2008; Momose *et al.*, 1996; Lundström *et al.*, 2014). As shown in Fig. 6(a), the outer membrane of the spinal cord parenchyma was visible in the PCI images but was not discernible in the ACI images. Furthermore, the degree of vessel visualization achieved with the ACI imaging model depends on the perfusion of the contrast agent, which may exert negative effects on the specimen, such as allergic reactions or death in response to the iodine injection (Matthews, 2015; Schopp *et al.*, 2013). However, using the PCI imaging model, the vessels could be distinguished without contrast agent perfusion. This imaging method has revolutionized the traditional method of vessel visualization. The detection of individual cells without the application of any stain is also feasible in the field of PCI imaging (Schulz *et al.*, 2010; Zehbe *et al.*, 2012). Additionally, the 3D microvascular network and the neuronal system in a mouse spinal cord could be detected at a high-resolution level through PCI imaging, which can be considered a new platform

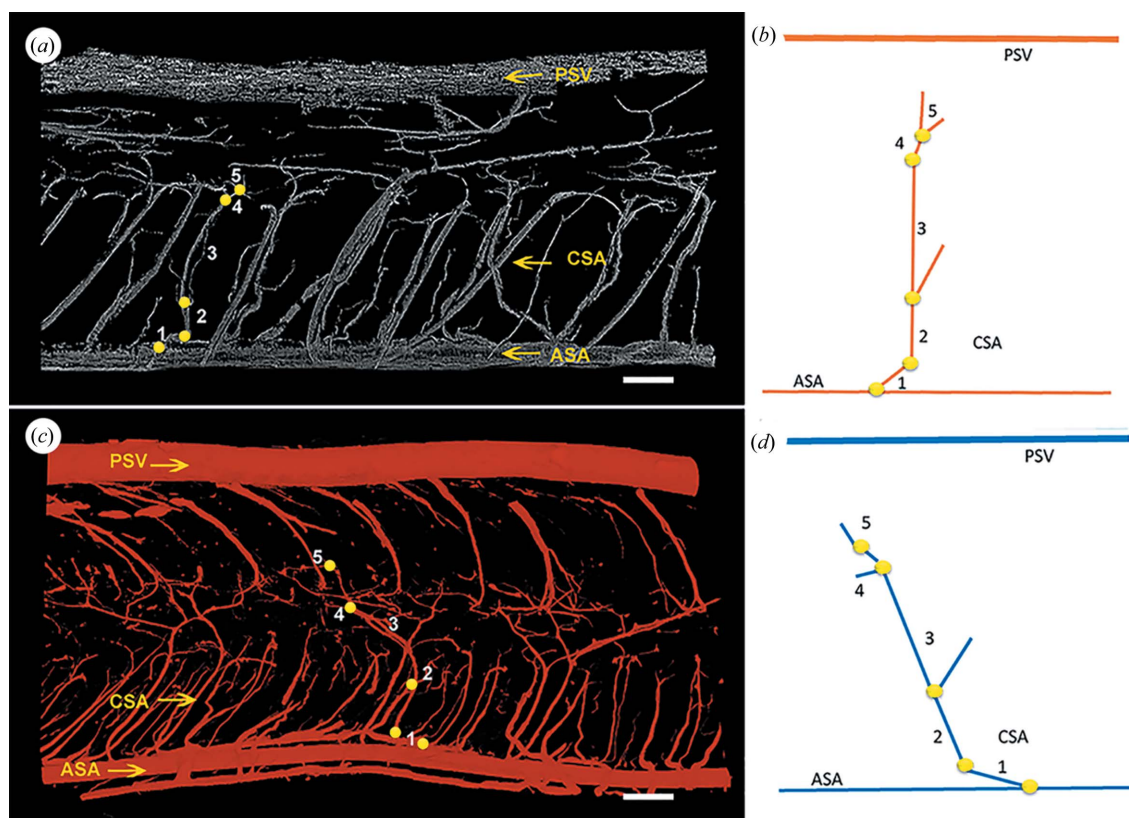


**Figure 7**  
Sagittal plane view of the CSA selected from PCI and ACI. (a) PCI image of the CSA. (c) ACI image of the CSA. (b), (d) Schematic depictions of the vessel classifications from (a) and (c). ASA refers to the anterior spinal artery, and PSV indicates the posterior spinal vein. CSA indicates the central sulcus artery. (a), (c) Scale bar =  $50 \mu\text{m}$ .

for clarifying the interactions and relationships between the vasculature and neural activity (Fratini *et al.*, 2015). Furthermore, the ACI model for vessel visualization requires contrast agent perfusion, and the penetration of this contrast agent into the smallest vessels is not always optimized due to the viscosity of the agent, which might limit the visualization of the smallest vessels. Vessel visualization by PCI relies on the edge enhancement of the vessel structure, which could be affected by artifacts introduced by a lack of phase retrieval, and these challenges remain to be overcome. The PCI imaging method was recently combined with CO<sub>2</sub> angiography for high-resolution vascular imaging in small animals and was shown to expose the specimens to a low radiation dose relative to that associated with conventional iodine-based ACI (Lundström *et al.*, 2012a,b). Compared with conventional X-ray imaging, low-dose PCI may become an important tool for the routine imaging of biomedical samples and might more closely mimic the desired clinical applications with fewer side effects (Zhu *et al.*, 2010).

Furthermore, using the developed segmented algorithm for PCI, we were able to depict the 3D morphology of the characteristic artery, the central sulcus artery of the spinal cord. This method provided vivid high-resolution images of this complex artery and even displayed its branches (Fig. 7). This accuracy was difficult to achieve with histological sections, in which the 3D complexities of the central sulcus artery were barely visualized. Additionally, although PCI and ACI have different imaging abilities for vessel detection, both exhibit significant correlations with the histological method, as determined in our study. These methods have been used in combination with histology for cerebellum visualization, the early diagnosis of breast cancer and hyaline cartilage imaging (Zhao *et al.*, 2012; Schulz *et al.*, 2010; Horg *et al.*, 2014). Although previous research studies have been conducted in this area, the 3D visualization of the intramedullary artery structure in the spinal cord by PCI and ACI combined with histological methods remains a challenge. Our research represents the first preclinical study to demonstrate that both PCI and ACI have the capability to accurately visualize the intramedullary artery and are thus potentially useful for the evaluation of microvascular changes in spinal cord diseases.

Although PCI and ACI present many advantages for vessel imaging, high-resolution imaging necessitates long scanning and exposure times, which inevitably results in the delivery of higher radiation doses to the specimen. Prior to the clinical application of these methods, researchers must focus on optimizing imaging parameters and decreasing the radiation doses required. In general, these methods are associated with high radiation doses, which need to be lowered as the techniques are further refined. Several other issues were noted during the evaluation of these techniques. During sample preparation, our specimens were dehydrated before imaging, resulting in the spinal cord exhibiting mild atrophy and altering the morphological features compared with their original state. Therefore, a true measurement of the vessel size was impossible. However, these procedures were performed using a similar protocol for spinal cord sample preparation;

thus, the tissue atrophy ratios are likely to be the same, and their comparison was not quantitatively biased.

## 5. Conclusions

In conclusion, both ACI and PCI imaging based on SR have the capability to visualize and clearly depict the 3D morphology of the intramedullary arteries of mouse spinal cord. Compared with ACI, PCI can detect the spinal cord vessels without contrast agent injection and might be a promising novel method with potentially broad preclinical applications, such as evaluating pathological changes in small vessels and clarifying their role in neurovascular disorders.

## Acknowledgements

This work was performed at the SSRF BL13W1, Shanghai, China, and supported by the National Natural Science Foundation of China (Nos. 81171698, 81301542 and 81371956) and Hunan Provincial Innovation Foundation For Postgraduate (No. CX2015B060). We thank Professor Tiqiao Xiao for kind assistance in SR imaging at the BL13W1 station.

## References

- Eggl, E., Schleede, S., Bech, M., Achterhold, K., Loewen, R., Ruth, R. D. & Pfeiffer, F. (2015). *Proc. Natl Acad. Sci. USA*, **112**, 5567–5572.
- Figley, S. A., Khosravi, R., Legasto, J. M., Tseng, Y. F. & Fehlings, M. G. (2014). *J. Neurotrauma*, **31**, 541–552.
- Fratini, M., Bukreeva, I., Campi, G., Brun, F., Tromba, G., Modregger, P., Bucci, D., Battaglia, G., Spanò, R., Mastrogiacomo, M., Requardt, H., Giove, F., Bravin, A. & Cedola, A. (2015). *Sci. Rep.* **5**, 8514.
- Gandhi, R., Curtis, C. M. & Cohen-Gadol, A. A. (2015). *J. Neurosurg.* **22**, 205–210.
- Garg, V., Manjila, S., Corriveau, M., Bambakidis, N. C. & Sunshine, J. L. (2015). *Clin. Imaging*, **39**, 677–681.
- Goto, N. & Otsuka, N. (1997). *Neuropathology*, **17**, 25–31.
- Horg, A., Brun, E., Mittone, A., Gasilov, S., Weber, L., Geith, T., Adam-Neumair, S., Auweter, S. D., Bravin, A., Reiser, M. F. & Coan, P. (2014). *Invest. Radiol.* **49**, 627–634.
- Hoshino, M., Uesugi, K., Tsukube, T. & Yagi, N. (2014). *J. Synchrotron Rad.* **21**, 1347–1357.
- Hu, J. Z., Wu, T. D., Zhang, T., Zhao, Y. F., Pang, J. & Lu, H. B. (2012). *J. Neurosci. Methods*, **204**, 150–158.
- Kerschensteiner, M., Schwab, M. E., Lichtman, J. W. & Misgeld, T. (2005). *Nat. Med.* **11**, 572–577.
- Kidoguchi, K., Tamaki, M., Mizobe, T., Koyama, J., Kondoh, T., Kohmura, E., Sakurai, T., Yokono, K. & Umetani, K. (2006). *Stroke*, **37**, 1856–1861.
- Koyanagi, I., Tator, C. H. & Lea, P. J. (1993a). *Neurosurgery*, **33**, 277–283.
- Koyanagi, I., Tator, C. H. & Lea, P. J. (1993b). *Neurosurgery*, **33**, 285–291.
- Lang, S., Müller, B., Dominietto, M. D., Cattin, P. C., Zanette, I., Weitkamp, T. & Hieber, S. E. (2012). *Microvasc. Res.* **84**, 314–322.
- Lewis, R. (1997). *Phys. Med. Biol.* **42**, 1213–1243.
- Lundström, U., Larsson, D. H., Burvall, A., Scott, L., Westermarck, U. K., Wilhelm, M., Arsenian Henriksson, M. & Hertz, H. M. (2012a). *Phys. Med. Biol.* **57**, 7431–7441.

- Lundström, U., Larsson, D. H., Burvall, A., Takman, P. A., Scott, L., Brismar, H. & Hertz, H. M. (2012b). *Phys. Med. Biol.* **57**, 2603–2617.
- Lundström, U., Westermark, U. K., Larsson, D. H., Burvall, A., Arsenian Henriksson, M. & Hertz, H. M. (2014). *Phys. Med. Biol.* **59**, 2801–2811.
- Martirosyan, N. L., Feuerstein, J. S., Theodore, N., Cavalcanti, D. D., Spetzler, R. F. & Preul, M. C. (2011). *J. Neurosurg. Spine*, **15**, 238–251.
- Matthews, E. P. (2015). *Radiol. Technol.* **86**, 623–638.
- Momose, A., Takeda, T., Itai, Y. & Hirano, K. (1996). *Nat. Med.* **2**, 473–475.
- Mori, H., Hyodo, K., Tanaka, E., Uddin-Mohammed, M., Yamakawa, A., Shinozaki, Y., Nakazawa, H., Tanaka, Y., Sekka, T., Iwata, Y., Handa, S., Umetani, K., Ueki, H., Yokoyama, T., Tanioka, K., Kubota, M., Hosaka, H., Ishikawa, N. & Ando, M. (1996). *Radiology*, **201**, 173–177.
- Myojin, K., Taguchi, A., Umetani, K., Fukushima, K., Nishiura, N., Matsuyama, T., Kimura, H., Stern, D. M., Imai, Y. & Mori, H. (2007). *Am. J. Neuroradiol.* **28**, 953–957.
- Niimi, Y., Matsukawa, H., Uchiyama, N. & Berenstein, A. (2015). *Am. J. Neuroradiol.* **36**, 1763–1768.
- Rubin, M. N. & Rabinstein, A. A. (2013). *Neurol. Clin.* **31**, 153–181.
- Schopp, J. G., Iyer, R. S., Wang, C. L., Petscavage, J. M., Paladin, A. M., Bush, W. H. & Dighe, M. K. (2013). *Emerg. Radiol.* **20**, 299–306.
- Schulz, G., Weitkamp, T., Zanette, I., Pfeiffer, F., Beckmann, F., David, C., Rutishauser, S., Reznikova, E. & Müller, B. (2010). *J. R. Soc. Interface*, **7**, 1665–1676.
- Stolz, E., Yeniguen, M., Kreisel, M., Kampschulte, M., Doenges, S., Sedding, D., Ritman, E. L., Gerriets, T. & Langheinrich, A. C. (2011). *Neuroimage*, **54**, 1881–1886.
- Suortti, P. & Thomlinson, W. (2003). *Phys. Med. Biol.* **48**, R1–R35.
- Tang, L., Li, G., Sun, Y.-S., Li, J. & Zhang, X.-P. (2012). *J. Synchrotron Rad.* **19**, 319–322.
- Tang, P., Zhang, Y., Chen, C., Ji, X., Ju, F., Liu, X., Gan, W. B., He, Z., Zhang, S., Li, W. & Zhang, L. (2015). *Sci. Rep.* **5**, 9691.
- Uotani, K., Yamada, N., Kono, A. K., Taniguchi, T., Sugimoto, K., Fujii, M., Kitagawa, A., Okita, Y., Naito, H. & Sugimura, K. (2008). *Am. J. Neuroradiol.* **29**, 314–318.
- Xuan, R., Zhao, X., Hu, D., Jian, J., Wang, T. & Hu, C. (2015). *Sci. Rep.* **5**, 11500.
- Yuan, R., Peters, L. L. & Paigen, B. (2011). *ILAR J.* **52**, 4–15.
- Zehbe, R., Riesemeier, H., Kirkpatrick, C. J. & Brochhausen, C. (2012). *Micron*, **43**, 1060–1067.
- Zhang, M. Q., Zhou, L., Deng, Q. F., Xie, Y. Y., Xiao, T. Q., Cao, Y. Z., Zhang, J. W., Chen, X. M., Yin, X. Z. & Xiao, B. (2015). *Sci. Rep.* **5**, 14982.
- Zhang, Z., Wang, H., Zhou, Y. & Wang, J. (2013). *Spinal Cord*, **51**, 442–447.
- Zhao, Y., Brun, E., Coan, P., Huang, Z., Sztórkay, A., Diemoz, P. C., Liebhardt, S., Mittone, A., Gasilov, S., Miao, J. & Bravin, A. (2012). *Proc. Natl Acad. Sci. USA*, **109**, 18290–18294.
- Zhou, S. A. & Brahme, A. (2008). *Phys. Med.* **24**, 129–148.
- Zhu, P., Zhang, K., Wang, Z., Liu, Y., Liu, X., Wu, Z., McDonald, S. A., Marone, F. & Stampanoni, M. (2010). *Proc. Natl Acad. Sci. USA*, **107**, 13576–13581.